ELSEVIER

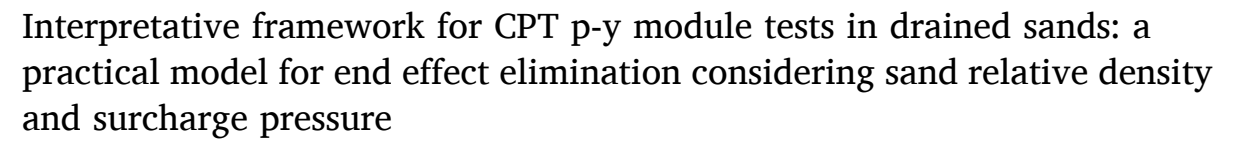
Contents lists available at ScienceDirect

# Computers and Geotechnics

journal homepage: www.elsevier.com/locate/compgeo



## Research Paper





Kai Wen <sup>a,\*</sup> <sup>o</sup>, David J. White <sup>a</sup>, Benjamin Cerfontaine <sup>a</sup> <sup>o</sup>, Susan Gourvenec <sup>a</sup> <sup>o</sup>, Andrea Diambra <sup>b</sup>

### ARTICLE INFO

### Keywords: Numerical modelling Offshore site investigation ROBOCONE p-y module Sands End effect p-y curves

### ABSTRACT

Accelerating the current timeline of offshore wind projects is imperative to achieve global decarbonisation plans. In response, a novel in-situ site characterisation tool ROBOCONE is being developed to make the geotechnical design of offshore pile foundations more efficient by directly providing lateral *p-y* response data, reducing the need for offshore sampling and onshore laboratory testing. This device expands the kinematic range of standard cone penetrometer testing by integrating a robotic cylindrical section capable of horizontal translation, referred to as a p-y module. However, due to the finite length of p-y module, it is necessary to quantify 'end effects' to accurately derive *p-y* curves from the direct measurements of the p-y module. This paper presents detailed three-dimensional finite element analyses of the p-y module in sands, utilizing a bounding surface elastoplastic model that accounts for variations in stress-strain behaviour due to relative density and stress level. The resulting end effect model is underpinned by a two-stage optimisation process that considers key factors such as overburden pressure and relative density. The model's predictive accuracy is proven through additional finite element analyses different to the calibration cases. The research outcomes offer a robust interpretative framework to accurately determine *p-y* curves for the design of laterally loaded offshore piles, using the ROBOCONE p-y module.

## 1. Introduction

The UK's long-term vision to achieve net-zero emissions necessitates up to 125GW offshore wind capacity to be installed by 2050 (Climate Change Committee, 2020), which is around seven times the current capacity of 15 GW at the end of 2023. To support this rapid growth, there is a pressing need to compress the typical timeline of offshore wind farm developments, which currently takes around 15 years from site leasing to operation in the UK (Greaves et al 2024). From the perspective of geotechnical practice, one of the crucial targets is enhancing the efficiency of the processes for site characterisation and design for offshore foundations.

Driven piles are commonly utilised as offshore foundations for bottom-fixed wind turbines and can also serve as anchors for offshore floating platforms. In current design practice, the serviceability response to lateral loads is typically predicted using the *p-y* spring approach. This approach involves dividing the pile into a series of segments and idealising the continuum soil domain into a series of independent nonlinear soil springs that represents the mobilisation of local lateral resistances, *p*, with local pile displacement, *y* (Matlock 1970; API 2014; DNV GL 2016; Burd et al. 2020; Jeanjean 2009). When establishing *p-y* curves at a specific site, it is common to correlate the cone penetration test (CPT) measurements to the stiffness and strength parameters needed for the *p-y* curves in advance of detailed soil laboratory testing (Suryasentana and Lehane 2014; Guo and Lehane 2016; Lehane 2019). However, it is recognised that the soil failure mechanisms and stress paths that govern CPT parameters do not match those controlling laterally pile-soil response parameters (Diambra et al. 2022).

A collaborative research project 'ROBOCONE' has developed a prototype of new site investigation tool by adding a cylindrical p-y module

E-mail addresses: k.wen@soton.ac.uk (K. Wen), david.white@soton.ac.uk (D.J. White), b.cerfontaine@soton.ac.uk (B. Cerfontaine), susan.gourvenec@southampton.ac.uk (S. Gourvenec), Andrea.Diambra@bristol.ac.uk (A. Diambra).

<sup>&</sup>lt;sup>a</sup> Department of Civil, Maritime and Environmental Engineering, University of Southampton, Southampton SO16 7QF, UK

<sup>&</sup>lt;sup>b</sup> Department of Civil Engineering, University of Bristol BS8 1TR Bristol, UK

<sup>\*</sup> Corresponding author.

section into the standard CPT equipment, as shown in Fig. 1 (White 2022; Diambra et al. 2022; Creasey et al., 2023). This device, capable of horizontal translation upon penetration into ground, expands the kinematic range of CPT testing and allows to probe the soil response to more representative stress histories, drawing on recent advancements in robotic control and actuation. This innovative equipment can accelerate the pile design process in two aspects: (i) by providing in-situ characterisation of soil properties, eliminating the challenges of sample disturbance and recapturing in-situ stress states during laboratory testing and (ii) direct extracting the *p-y* curves to support the design of laterally loaded piles, relying on the similarity of the soil deformation pattern near the *p-y* module and a pile elements (see Fig. 1). Wen et al. (2024) adopted approach (i) via an interpretive framework to convert measured ROBOCONE data into undrained clay's properties such as undrained shear strength and elastic stiffness.

This paper will tackle the approach (ii) and address the challenge of additional soil reaction due to the finite length of the p-y module and the resulting displacement discontinuity between the stationary penetrometer shaft and the moveable p-y module – referred hereafter as the end effect. It is necessary to eliminate such end effect from the p-y module measurements in order to obtain practical *p-y* curves for the design of laterally loaded piles.

Finite element (FE) modelling has been widely used to develop interpretative frameworks for novel in-situ characterisation tools, including T-bar penetrometers (Randolph and Andersen 2006, Wang et al., 2020), ball penetrometers (Zhou et al. 2013; Mahmoodzadeh et al. 2015) and shallow penetrometers – such as the hemiball and toroidal (Yan et al. 2011, Stanier & White, 2015). Given that the ROBOCONE p-y module is still a new concept, this paper contributes the first analyses of such a device in drained cohesionless material.

The objective of this paper is to develop an interpretative framework of accurately predicting, and eliminating, the end resistance contribution to the measured resistance on a p-y module in drained sands, thus providing the resistance equivalent to the p-y spring. Three-dimensional FE modelling of a p-y module subject to monotonic lateral movement is carried out, including a comprehensive parametric study with a wide range of device geometries and soil conditions, including variations in density, and overburden or surcharge pressure. The resulting end effect model allows the deduction of end resistance from p-y module measurements thus providing rational *p-y* curves for offshore pile design.

### 2. FINITE ELEMENT MODEL

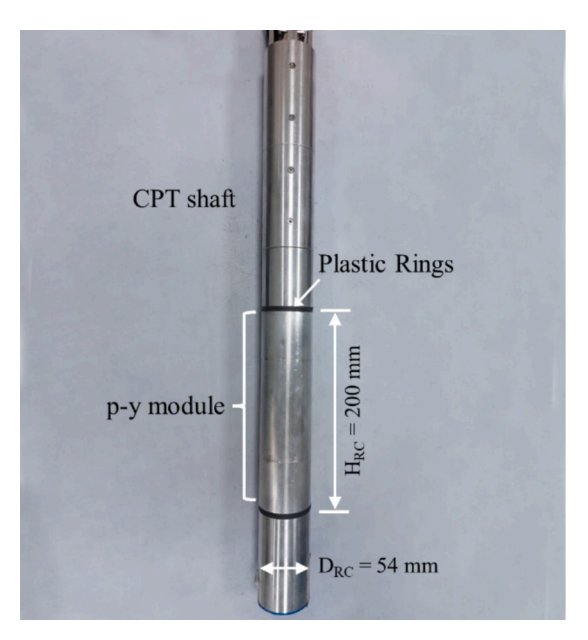
## 2.1. Model geometry and boundary conditions

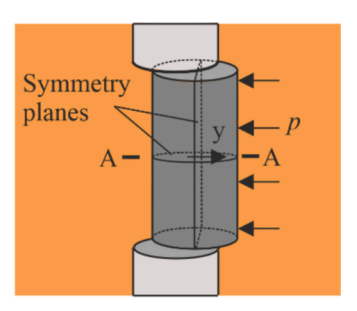
The three-dimensional finite element analyses in this study were carried out in the PLAXIS 3D V23 programme (PLAXIS, 2023). Fig. 2 illustrates the geometry of the ROBOCONE system, including the CPT shaft and moveable p-y module. These structures are wished-in-place, neglecting the impact of the installation process. In the prototype ROBOCONE, a stack of moveable discs is installed at each end of the p-y module to prevent water leakage and soil particles from entering the CPT rod (Creasey et al. 2023). However, these discs were omitted in this study in order to improve the numerical stability of FE analyses. Trial analyses indicate this simplification has a negligible impact on the ROBOCONE load–displacement response.

Benefiting from the double symmetry feature of the simulated problem (see Fig. 1), only a quadrant of p-y module was simulated to reduce the computational cost while ensuring numerical accuracy. Although the actual p-y module prototype is a hollow cylindrical shaft with a complex actuation system and sensors inside (Creasey et al. 2023), it was modelled as a solid rigid body herein for simplicity as the mechanical operation of the device is irrelevant for the analysis of the soil response. The prototype p-y module, featured an external diameter  $(D_{\rm RC})$  of 54 mm and a height  $(H_{\rm RC})$  of 100 mm, is embedded within a half-cylindrical soil domain measuring 2600 mm in diameter and 1100 mm in thickness. These soil dimensions were determined after trial sensitivity studies of possible domain boundary effect on p-y module response. It is important to note that any variations in the module dimensions ( $H_{RC}$ ,  $D_{RC}$ ), as discussed subsequently, require corresponding alterations in the dimensions of soil domain to efectively avoid any boundary effects.

The soil was discretised using second-order tetrahedral elements, each with 10-nodes and 4 Gaussian integration points. A relatively finer discretisation was applied near the p-y module to avoid stress concentrations and reduce the influence of element size. Two planes of symmetry at Y=0 and Z=0 were normally fixed to prevent orthogonal movements, while vertical displacements were permitted along the curved side of the soil domain and at the top surface.

The ROBOCONE system was modelled as a rigid body with all degrees of freedom fixed, except for a lateral translation in the X-direction which was prescribed. The stress–strain response of the soil material was





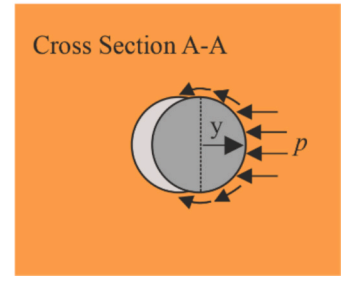


Fig. 1. Schematic illustration of ROBOCONE p-y module and testing mechanism (adapted from Diambra et al. 2022)

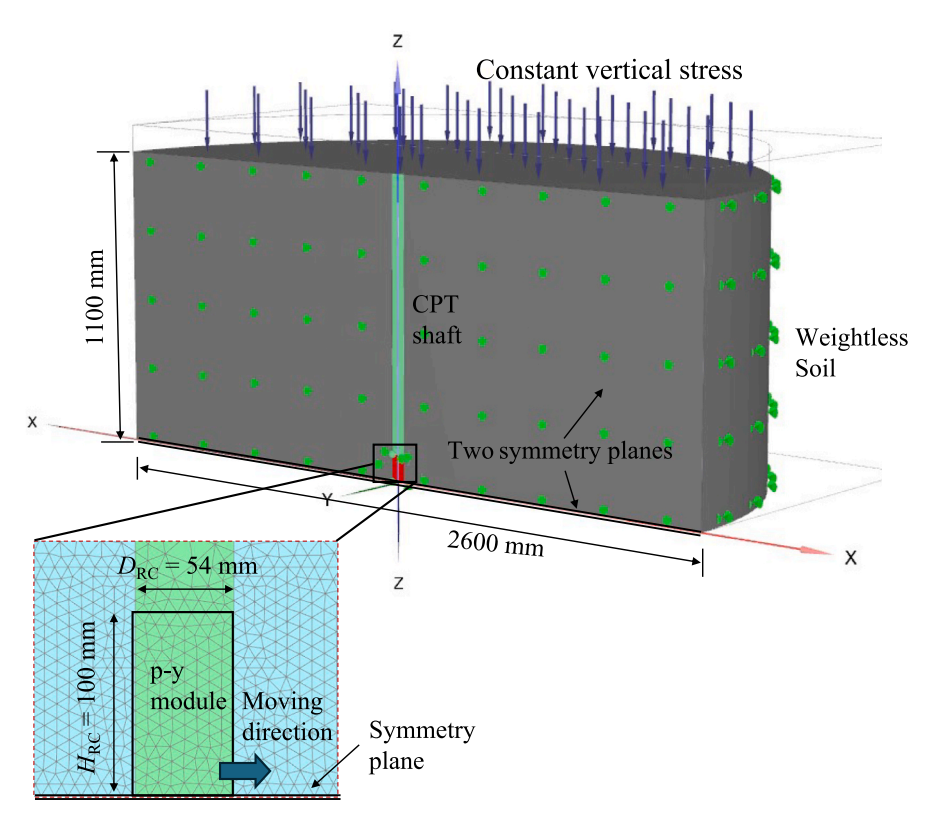


Fig. 2. Finite element model of the p-y module prototype ( $H_{RC}/D_{RC} = 3.7$ ) embedded in drained sands assembly with mesh, loading and boundary conditions.

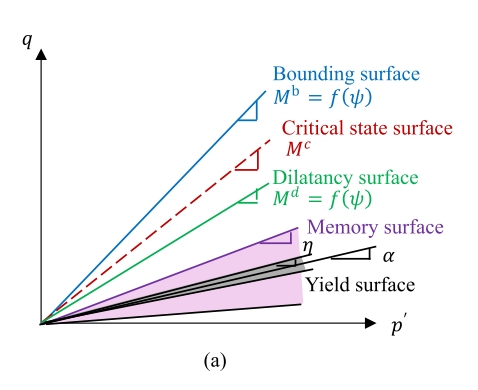
represented by a bounding surface plasticity model in fully drained conditions, as detailed later. Special zero-thickness interface elements were introduced around the p-y module to reflect the soil-structure interaction, which allows separation between the structure and soil to occur (PLAXIS, 2023). The interface was modelled using an elastoplastic Mohr-Coulomb model, with the elastic parameters of shear stiffness  $K_s = 4.5E6 \text{ kN/m}^3$  and normal stiffness  $K_n = 5.1E7 \text{ kN/m}^3$ . These stiffness parameters were determined after a sensitivity study that ensured they have negligible influence on the p-y module response. The plastic parameters included a nominal cohesion of  $c_i = 3 \text{ kPa}$  (ensuring numerical stability) and an effective angle of shearing resistance  $\varphi_i' = 29.0$ .

## 2.2. Constitutive model

The SANISAND-MS constitutive model (Liu et al. 2019) was selected to represent the drained sand stress strain behaviour. It is a bounding surface elastoplastic model, based on a critical state framework. The

model is a recent evolution of the parent SANISAND04 model (Dafalias and Manzari 2004) to accurately capture the sand response under long-term cyclic loading. It has been preferred over the parent model due to its enhanced versatility for future studies of the ROBOCONE p-y module under complex and cyclic loading paths. Nevertheless, the response under monotonic loading is identical to that of the parent SANISAND04 model. The monotonic plastic response is governed by four distinct conical surfaces (Fig. 3). They are (1) the yielding surface, controlling the boundary of the elastic region; (2) the dilatancy surface, defining the transition from plastic contraction to dilation; (3) the critical state surface, defining the stress conditions at failure and (4) the bounding surface, defining the peak strength and the plastic strain rate. This SANISAND models' family captures the effect of void ratio and mean effective stress, p', on strength and stiffness with a single set of parameters.

The model adopts a hypoelasticity law for its elastic behaviour, where the elastic shear and bulk modules ( $G_0$  and K) are functions of mean effective stress p' and current void ratio e (Li and Dafalias, 2002).



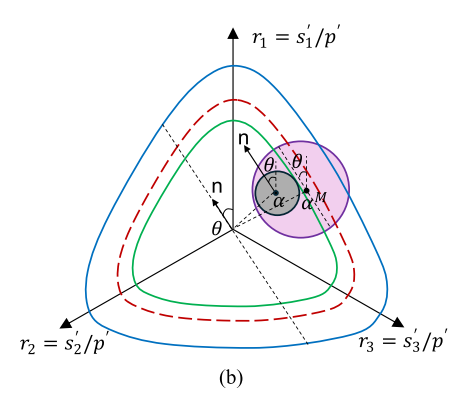


Fig. 3. Schematic illustration of SANISAND-MS model surfaces (a) in p-q space; (b) in the deviatoric stress ratio plane (modified after PLAXIS (2023)).

$$G_0 = G_0 p_{\text{atm}} \left[ \frac{(2.97 - e)^2}{(1 + e)} \right] \sqrt{\frac{p}{p_{\text{atm}}}}$$
 (1)

$$K = \frac{2}{3} \left( \frac{1+\nu}{1-2\nu} \right) G_0 \tag{2}$$

where  $G_0'$  is a dimensionless input parameter;  $\nu$  is a constant Poisson's ratio.

There are 11 primary model parameters employed to characterise the plasticity component of the SANISAND-MS model under monotonic loading and three additional parameters governing the response under cyclic loading. These parameters and the main modelling features are briefly introduced below:

- (a) The yield surface is a narrow cone in stress space, of a constant opening defined by the model parameter *m*. When the soil starts yielding, the inclination of the yield locus can change to maintain the soil stress state on its boundary. Consequently, the elastic region moves together with the changes in the mobilised stress ratio, as the model utilises only kinematic hardening.
- (b) The opening of the critical state surface is defined by the stress ratios q/p' corresponding to the strengths in triaxial compression and tension at critical state, denoted as  $M_{\rm e}$  and  $M_{\rm c}$  respectively. The model parameter c defines the ratio of  $M_{\rm e}/M_{\rm c}$ .
- (c) The opening of the bounding surface ( $M^b$ ) influences the peak strength of sand, and it is related to opening of the critical state surface through the state parameter  $\psi$ , defined as the difference between the current void ratio, e, and that at the critical state line ( $e_{cs}$ ) under the same p', as given by:

$$\psi = e - e_{\rm CS} = e - \left[ e_0 - \lambda \left( \frac{\dot{p}}{p_{\rm atm}} \right)^{\xi} \right]$$
 (3)

where the model parameter  $e_0$  represents the void ratio at the critical state for p'=0;  $\xi$  and  $\lambda$  are input parameters that control the shape of the critical state line in the e-ln p' plane (Dafalias & Manzari 2004). Hence, the opening angle of the bounding surface in triaxial compression is:  $M^b = M_c \bullet \exp \left( \langle -\psi \rangle n^b \right)$ , where  $n^b$  is an input parameter. Note that  $\langle -\psi \rangle = -\psi$  if  $\psi < 0$  and  $\langle -\psi \rangle = 0$  if  $\psi > 0$ . For very dense sands  $\psi$  is generally a large negative number, which allows a very high stress ratio to characterise the bounding surface, thus providing a high peak strength.

- (d) The dilatancy (i.e. the ratio between plastic volumetric strain and plastic deviatoric strain) depends on the deviatoric distance between the current stress state and the dilatancy surface and a model parameter  $A_0$ . This means the soil contracts when inside the dilatancy surface and dilates outside. A dilatancy surface with inclination  $M^d$  in the p'-q plane depends also on  $\psi$  and an input parameter  $n^d$ , as given by  $M^d = M_c \cdot \exp(n^d \psi)$  in compression. For dense sands, a large negative  $\psi$  yields a lower stress ratio, implying the onset of plastic dilation occurs early during shearing.
- (e) The plastic modulus depends on the deviatoric distance from the current stress state to the bounding surface, thus dependent on the current e and p, and scaled by the model parameters  $h_0$  and  $c_h$ .
- (f) There are three input parameters  $\mu_0$ ,  $\zeta$ ,  $\beta$  related to memory surfaces and the ratcheting characteristics of sands, but they should have no influence on the mechanical response in drained monotonic loading conditions.

# 2.3. Calibration of model parameters

The value of the model parameters previously calibrated by Pisanò et al. (2024) for the simulation of monopiles in the Dunkirk sands were

used in this study (see Table 1). Among those, the three parameters related to the memory surface are not considered to affect the monotonic loading behaviour of ROBOCONE module. The initial void ratio ( $e_0$ ) is specified as 0.6 (corresponding to  $D_R=83\%$ ) as a baseline case, which is later varied to investigate its effect of sand density on the p-y module response. The maximum and minimum void ratios were defined as the limits to the evolution of void ratio (Kuwano, 1999) to prevent unrealistic soil states.

Fig. 4 describes the performance of the SANISAND-MS model with the set of parameters from Table 1 against measured drained triaxial tests on Dunkirk sand at relative density  $D_{\rm R}=73\%$ . The results demonstrate reasonable agreement between the simulations and laboratory results (Zdravkovic et al., 2020), underscoring the effectiveness of the constitutive model across a range of initial confining stresses.

### 2.4. Description of FE simulations

For modelling the p-y module, the initial simulation phase created an isotropic stress state in the soil domain by applying a uniform vertical surcharge pressure on the top boundary surface of the soil domain (see Fig. 2) and specifying a coefficient of earth pressure at rest ( $K_0=1$ ) to generate horizontal stress. The soil was defined as weightless so that the variations of surcharge pressure ( $\sigma'_{\rm v}$ ) on the domain represented different overburden stresses at the operating depth of the p-y module. In the second simulation phase, lateral displacement of the p-y module was prescribed in the X direction.

The main objective of the FE analyses is to quantify end effects due to the finite length of ROBOCONE p-y module. To achieve this, two different types of simulation were undertaken, as illustrated in Fig. 4.

- Case A, consistent with the field conditions: a lateral monotonic displacement along the X-direction is prescribed to the reference point of the rigid p-y module, while the CPT shaft is fixed in all degrees of freedom.
- Case B: a lateral monotonic displacement along the X-direction is
  prescribed to the reference points of both the rigid p-y module and
  the CPT shaft, ensuring zero relative displacement between the
  moveable p-y module and the CPT shaft. By doing so, the end effects
  is rigorous removed.

In both cases, the resultant reaction force acting on the ROBOCONE p-y module were directly extracted at the reference points of horizontal translation, which corresponds to the total force  $F_{\rm tot}$  in the Case A and to the net force  $F_{\rm net}$  in the Case B. The reaction forces were then divided by the ROBOCONE projected area ( $D_{\rm RC}H_{\rm RC}$ ) to obtain the p-values, as illustrated in Fig. 5, denoted as  $p_{\rm tot}$  and  $p_{\rm net}$  in Case A and Case B respectively. In comparison to the Case A, the  $p_{\rm net}$ -y curves from Case B were considered to contain zero end effects, given there is no relative motion between ROBOCONE p-y module and CPT shaft. As such, the soil layers above and below the p-y module exhibits negligible interaction with the soil zone at the elevation of the module because their horizontal

Table 1
SANISAND-MS model parameters calibrated for Dunkirk sands (Pisanò et al. 2024) as used in this study.

Components	Parameters
Elasticity	$G_0 = 451; \nu = 0.17$
Critical state line	$M_c = 1.28$ ; $c = 0.72$ ; $\lambda_c = 0.135$ ; $e_0 = 0.91$ ; $\xi = 0.18$
Yield surface	m = 0.065
Hardening modulus	$h_0 = 3.5$ ; $c_h = 1.0$ ; $n_b = 1.9$
Dilatancy	$A_0 = 1.3; n_d = 0.75$
Memory surface	$\mu_0 = 260; \zeta = 1\text{E-4}; \beta = 1.0$
Initial void ratio	$e_0 = 0.60$
Min and Max void ratios	$e_{min} = 0.54$ ; $e_{max} = 0.91$
Maximum bounding stress ratio	$M_{\text{max}}^{\text{b}} = 1.63$

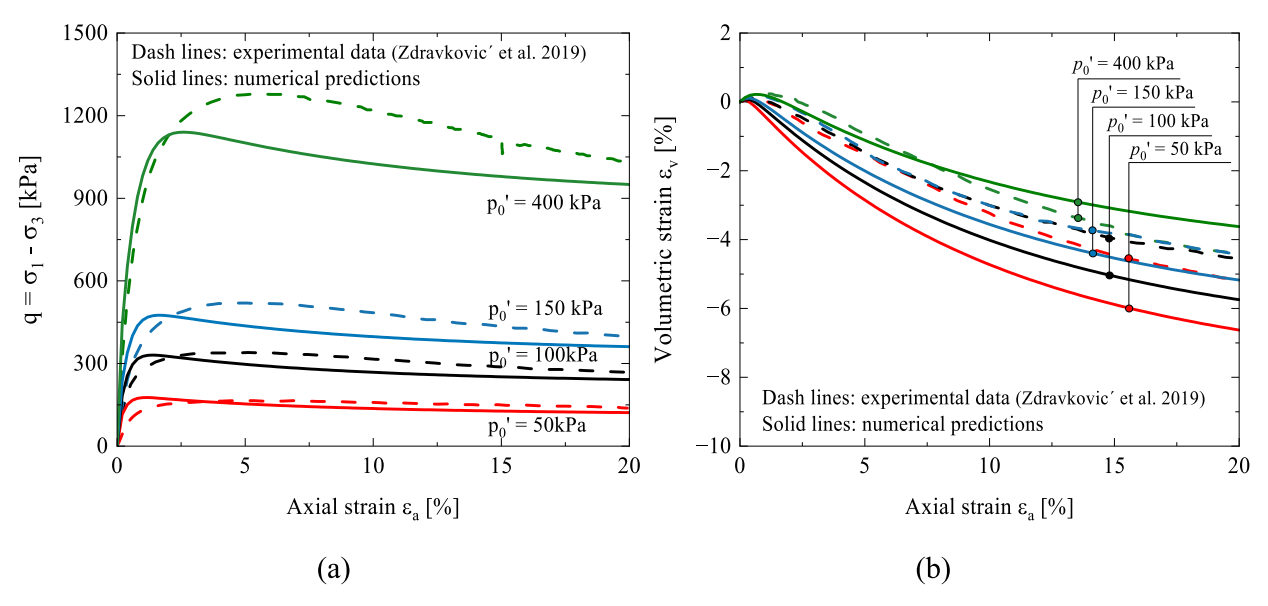


Fig. 4. Performance of SANISAND-MS model on predicting the drained triaxial compression behaviour of Dunkirk sand (adapted from Pisanò et al. 2024)

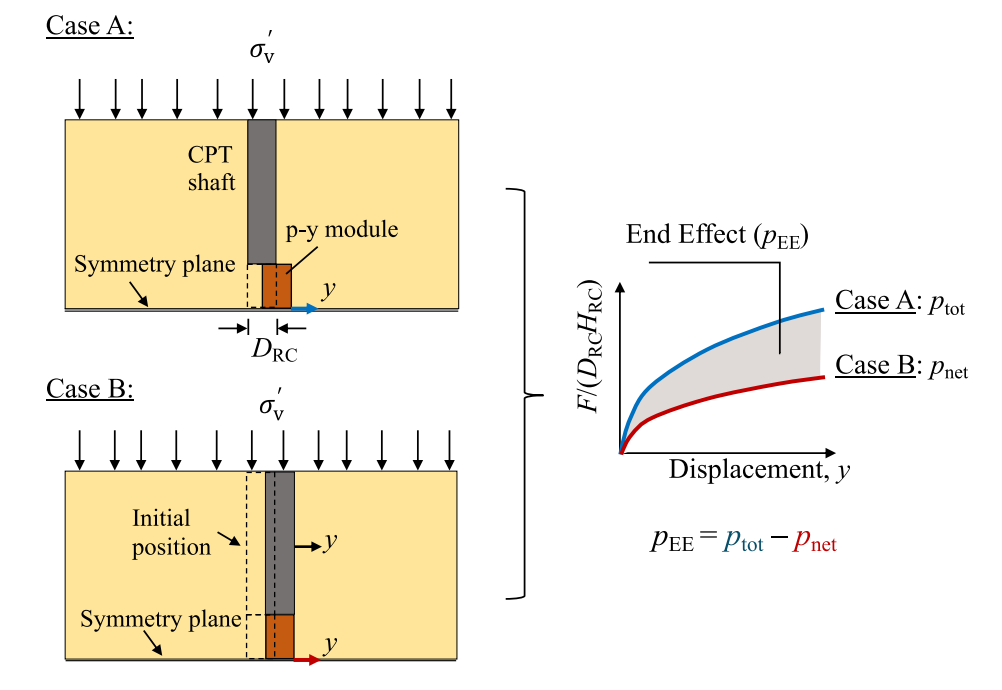


Fig. 5. Determination of end effects from comparison of FE analysis cases.

movements are equal. This aligns well with the original definition of the p-y approach, in which the soil domain is idealised into a series of independent Winkler-type springs acting on the lateral piles (Reese et al. 1974). Hence,  $p_{\rm net}$ -y curves in the Case B are what the users of ROBO-CONE need in order to design offshore laterally loaded piles.

As seen in Fig. 5, the total ROBOCONE resistances (Case A) are therefore the superposition of two components, i.e. the net ROBOCONE resistance (Case B) plus the additive resistances due to end effect  $p_{\rm EE}$ , so that

$$p_{\rm EE} = \frac{F_{\rm tot} - F_{\rm net}}{D_{\rm RC} H_{\rm RC}} = p_{\rm tot} - p_{\rm net} \tag{4}$$

### 3. Results & discussion

The mechanisms related to end effects of the ROBOCONE p-y modules are first identified, and the main influencing parameters discussed, including aspect ratio ( $H_{\rm RC}/D_{\rm RC}$ ), sand relative density ( $D_{\rm R}$ ) and surcharge pressure ( $\sigma_{\rm v}$ ). Afterwards, an interpretative framework is developed based on a parametric study for the p-y module with aspect ratio  $H_{\rm RC}/D_{\rm RC}=3.7$ , which corresponds to the prototype ROBOCONE (Creasey et al., 2023).

## 3.1. Key features of ROBOCONE p-y module response

Aspect ratio is an important geometric feature of the ROBOCONE. A high aspect ratio reduces the relative contribution of the end effect to the

measured total force, which is beneficial. However, the force required to move the p-y module increases with its length and is limited by the capacity of the actuation system that has to be miniaturised in order to fit in the standard CPT rod.

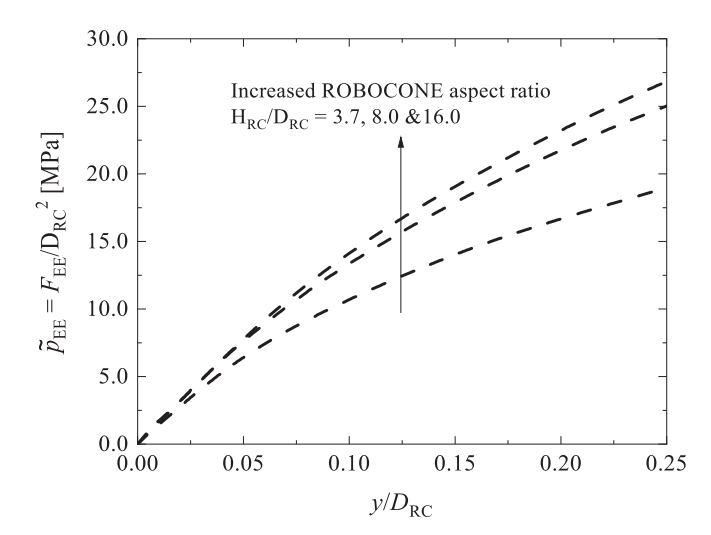
Fig. 6 illustrates the numerical total resistances ( $p_{tot}$ , Case A) and net resistances ( $p_{net}$ , Case B) of ROBOCONE and the calculated end effect ( $p_{EE}$ , Eq. (4)), for a selected surcharge pressure  $\sigma'_v = 200$  kPa and relative density  $D_R = 83\%$ . The p-y module reaction forces are divided by the product of the height and diameter of the ROBOCONE module,  $H_{RC}D_{RC}$ , and the lateral displacement is normalised by  $D_{RC}$ . Three different aspect ratios,  $H_{RC}/D_{RC} = 3.7$  (prototype), 8.0 and 16.0, were tested.

Fig. 6 shows the total resistance ( $p_{\rm tot}$ ) decreases with the aspect ratio. However, the  $p_{\rm net}$ -y curves are almost identical, regardless of the aspect ratio of the ROBOCONE. The relative contribution of the end effect to the ROBOCONE  $p_{\rm tot}$  appear to vary as a function of the aspect ratio. For instance, the ratio of  $p_{\rm EE}/p_{\rm tot}$  at  $y/D_{\rm RC}=35\%$  reduces from 39% for the shortest p-y module ( $H_{\rm RC}/D_{\rm RC}=3.7$ ) to 20% for the longest p-y module ( $H_{\rm RC}/D_{\rm RC}=16.0$ ). Moreover, the relative importance of the end effects in the measured ROBOCONE resistances ( $p_{\rm tot}$ ) tend to vary as a function of the normalised  $y/D_{\rm RC}$ . At small displacement, the net resistance component ( $p_{\rm net}$ ) dictates the magnitudes of total resistances, while the end effects become more prominent in a later stage of the p-y module displacement. Therefore, any end effect correction of the measured ROBOCONE data should include this dependency.

The resistance  $p_{\rm EE}$  above is expressed as the calculated end effect force  $F_{\rm EE}$  divided by the projected area of ROBOCONE ( $H_{\rm RC}D_{\rm RC}$ ) in the translating direction. As with Wen et al. (2024), another more meaningful and straightforward way is to present end resistances in the form of  $\widetilde{p}_{\rm EE} = F_{\rm EE}/D_{\rm RC}^2$ , which excludes the impact of the ROBOCONE length so is a better quantity to describe the end effect. By doing so, the Fig. 6(c) can be converted to investigate relationship between  $\widetilde{p}_{\rm EE}$  and aspect ratio. As shown in Fig. 7, the evolution of  $\widetilde{p}_{\rm EE}$  tend to converge at greater  $H_{\rm RC}/D_{\rm RC}$ , which implies some degree of interaction between the two ends for lower aspect ratios.

Fig. 8 demonstrates the influence of surcharge pressure  $(\sigma'_v)$  on the py module response components, of total, net and end resistances respectively. Higher stress levels lead to increased resistance and initial stiffness, as captured in the SANISAND-MS model by the frictional nature of soil resistance and the stress dependent soil stiffness defined in Eq. (1). The contribution of the end effect  $(p_{\rm EE})$  to the total ROBOCONE resistance  $(p_{\rm tot})$  decreases with an increasing surcharge stress  $\sigma'_v$ . For instance, at a normalised displacement  $y/D_{\rm RC}=30\%$ , the end effect accounts for approximately 50% of the total resistance at low surcharge stress  $\sigma'_v=10$  kPa, reducing to around 40% at  $\sigma'_v=200$  kPa.

While most p-y models for pile design include a plateau in  $\boldsymbol{p}$  values in



**Fig. 7.** Variation of end resistance with increasing lateral displacement and ROBOCONE p-y module aspect ratios ( $\sigma_{\rm v}^{\prime}=200~{\rm kPa}$ ).

drained sands (e.g., API 2014; Burd et al. 2020), the only simulation that reached a stable upper limit of  $p_{RC}$  was for a surcharge stress  $\sigma'_{v} = 10$ kPa, at a displacement of  $25\%D_{RC}$ , which approaches the lateral translation limit of the prototype ROBOCONE, which is  $20\%\sim25\%D_{RC}$ (Creasey et al., 2023). This effect can be attributed to the progressive suppression of the soil's tendency to dilate during shearing due to the confining pressure from the surrounding mass. As the soil tends to dilate within a confined mass, the surrounding confining stress increases, leading to a corresponding increase in the soil's shear strength. This process continues until the shear strength reaches a plateau when the soil attains its critical state conditions. This increase will be higher and take longer for deep embedment depth ( $\sigma'_v = 200 \text{ kPa}$ ) due to the higher soil stiffness and larger volume of surrounding soil mass involved. Indeed, the plateaus observed in p-y curves backfitted to full-scale pile load tests are located close to the surface (at low vertical stress), where a shallow mechanism develops. It can therefore be assumed that the variation of surcharge pressure is a simple way to represent the change in response of the p-y module at different operation depths.

# 3.2. End effect mechanism

The vertical soil displacement during translation of the p-y module is an indicative way to show the influence zone and three-dimensional nature of the end effects. Fig. 9 shows the profile of soil displacement

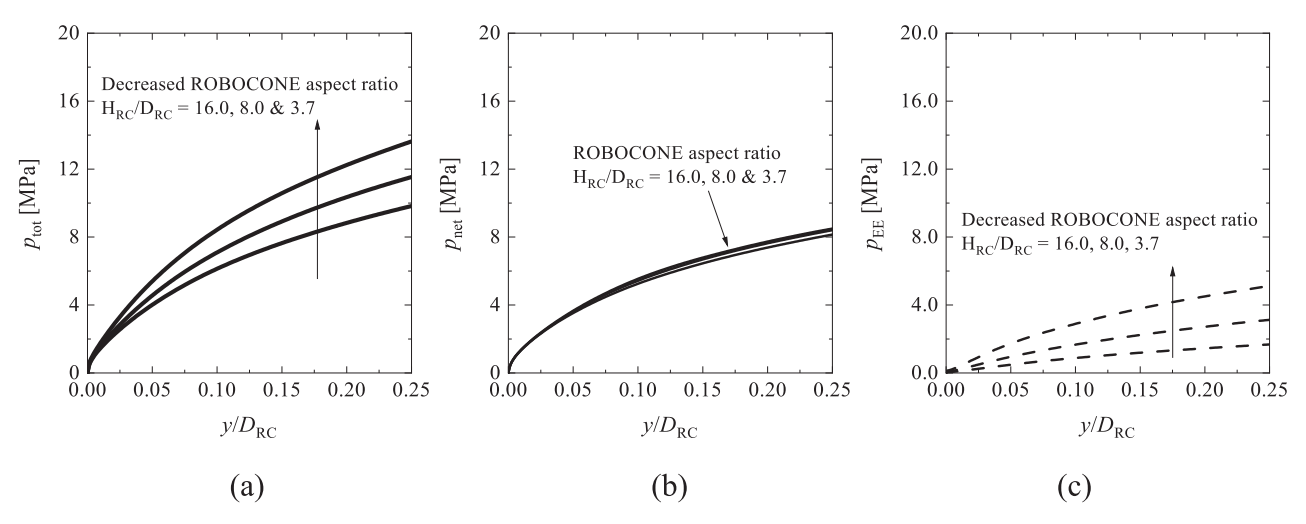


Fig. 6. Monotonic loading response of various p-y modules ( $\sigma_{v}^{'}=200~\text{kPa}$ ;  $D_{R}=83\%$ ): (a)  $p_{\text{tot}}$ -y curves; (b)  $p_{\text{net}}$ -y curves; (c)  $p_{\text{EE}}$ -y curves.

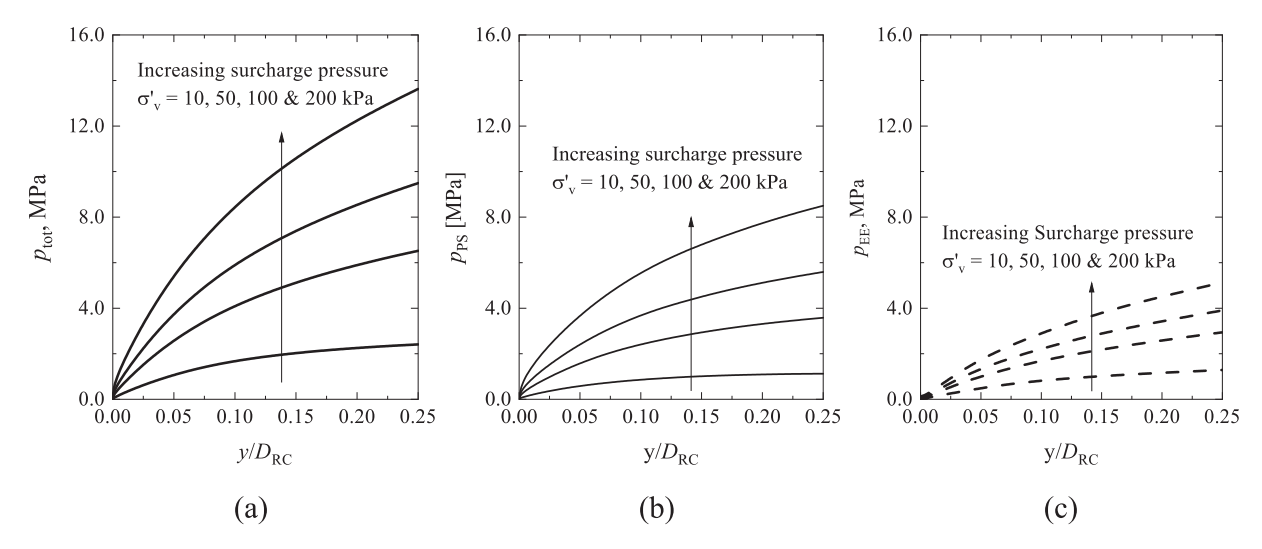


Fig. 8. Impact of surcharge pressure  $\sigma_{\rm v}$  on the p-y module response ( $H_{\rm RC}/D_{\rm RC}=3.7;\,D_{\rm R}=83\%$ ): (a) total resistances  $p_{\rm tot}$ ; (b) net resistances  $p_{\rm net}$ ; (c) end effect resistances  $p_{\rm EE}$ .

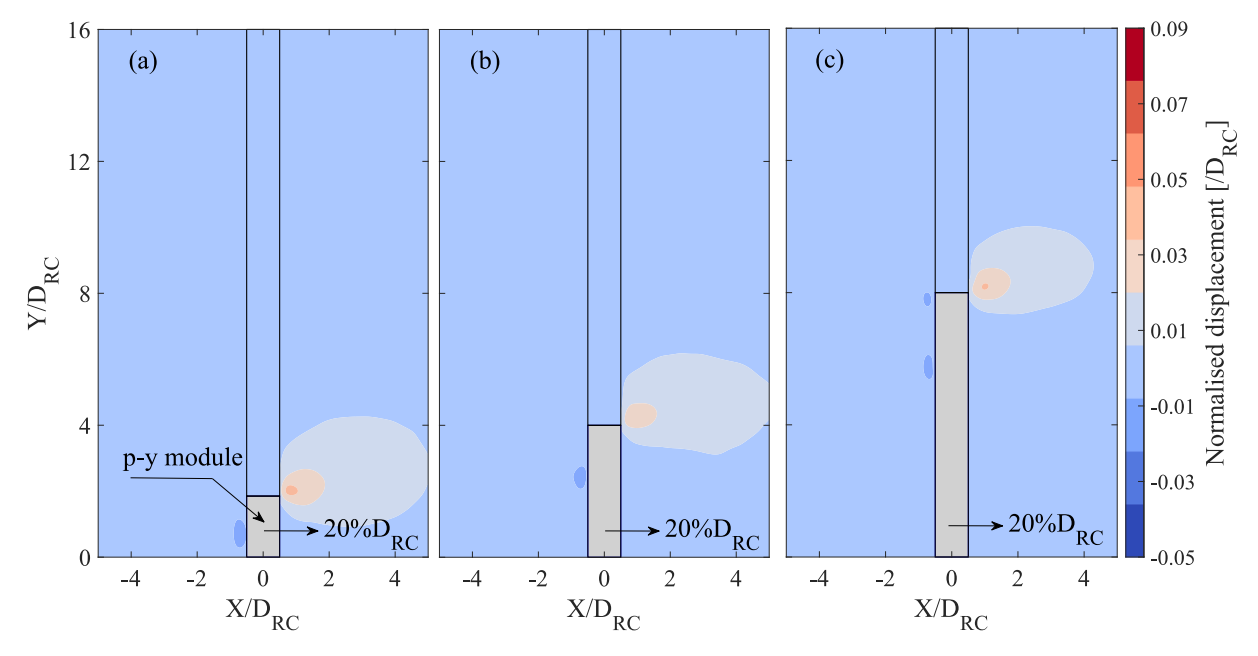


Fig. 9. Fields of cumulative vertical soil displacement at the p-y module displacement of  $y/D_{RC} = 20\%$ : (a)  $H_{RC}/D_{RC} = 3.7$ ; (b)  $H_{RC}/D_{RC} = 8.0$ ; (c)  $H_{RC}/D_{RC} = 16.0$ .

in the symmetry plane of the p-y module at a displacement of  $20\%D_{\rm RC}$ , with  $H_{\rm RC}/D_{\rm RC}=3.7$ , 8.0 and 16.0. The zones of vertical displacement retain a similar shape independent of the aspect ratios, while their dimensions show slight variations. Those vertical displacement zones overlap with the volume of soil directly in front of the p-y module and indicate that some degree of interaction exists between the two p-y components ( $p_{\rm EE}$  and  $p_{\rm net}$ ). The vertical displacement of the soil closer to the symmetry line is close to zero, especially at larger aspect ratios.

Fig. 10 shows the distribution of current void ratio surrounding the p-y module at the longitudinal cross section (y=0). The void ratio is incorporated as a state variable in the SANISAND-MS model and capable of visualising the soil zones influenced by the p-y module movement. The sand domain at the front of the p-y module experiences dilation, i.e., an increase in void ratio (relative to initial  $e_0=0.60$ ), owing to the dilation of the dense sand (initially  $D_{\rm R}=83\%$ ). Behind the p-y module, where the soil is experiencing unloading, an increase in void ratio can be observed for all cases.

## 3.3. End effect model

The purpose of the ROBOCONE tool is to determine  $p_{\text{net}}$ -y curves directly in situ. This requires correction of the measured  $p_{\text{tot}}$ -y curves to remove the end effect contribution across the full range of lateral displacements. The following section details this correction framework for monotonic loading, for the aspect ratio corresponding to the dimensions of the prototype p-y module ( $H_{\text{RC}}/D_{\text{RC}}=3.7$ ) (Creasey et al., 2023).The calibration space, as set out in Table 2, consisting of 12 combinations of surcharge pressure ( $\sigma'_{\text{v}}$ , from 10 kPa to 200 kPa) and relative densities ( $D_{\text{R}}$ , from 43% to 83%). For each combination, a pair of FE analyses were undertaken (Cases A and B), to calculate the end effect contribution  $\widetilde{p}_{\text{EE}}$ . All individual curves were fitted by an explicit conic function (Equations (5), (6)), which has been used to capture the p-y soil response from small to large displacements and has been widely adopted by the offshore industry (Burd et al. 2020).

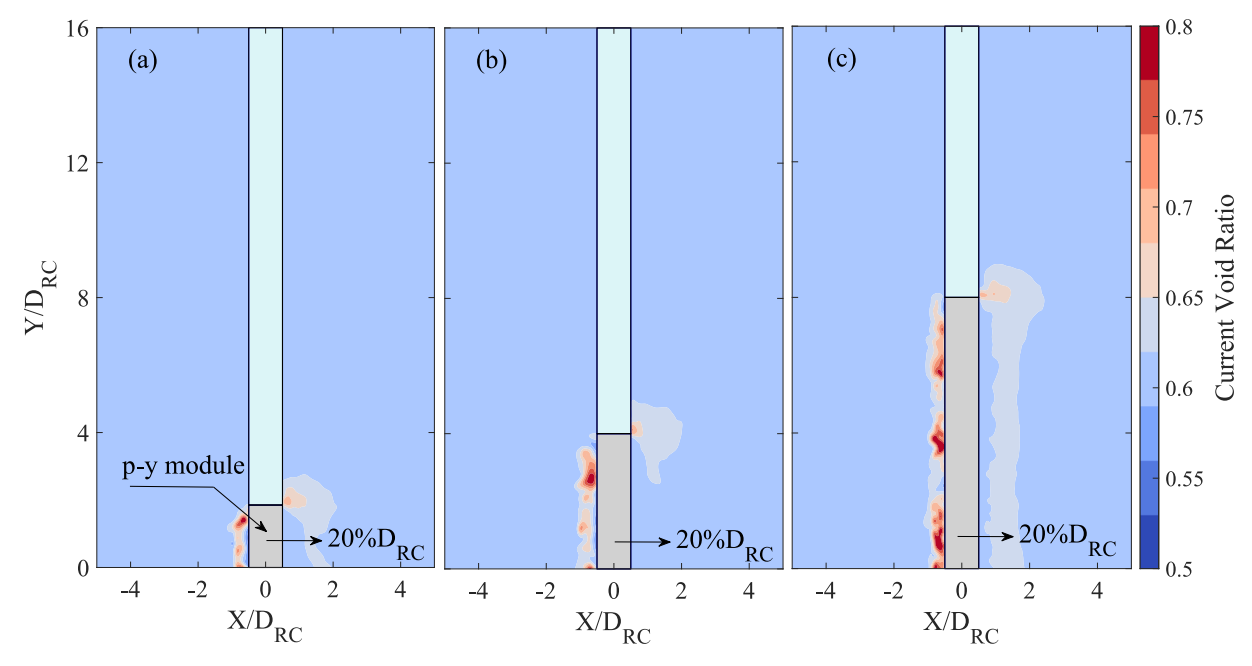


Fig. 10. Fields of current soil void ratio at the p-y module displacement of  $y/D_{RC}=20\%$ : (a)  $H_{RC}/D_{RC}=3.7$ ; (b)  $H_{RC}/D_{RC}=8.0$ ; (c)  $H_{RC}/D_{RC}=16.0$ .

Table 2 Calibration space encompassed by 12 combinations of surcharge pressure  $(\sigma_v')$  and relative density  $(D_R)$ .

$D_{\mathrm{R}}$	$\sigma_{ m v}^{\prime} [{ m kPa}]$	$D_{R}$	$\sigma_{ m v}^{\prime}[{ m kPa}]$	$D_{\mathrm{R}}$	$\sigma_{\mathrm{v}}^{\prime}[\mathrm{kPa}]$
83%	10	65%	10	43%	10
	50		50		50
	100		100		100
	200		200		200

$$\widetilde{p}_{\text{EE}} = \widetilde{p}_{\text{u,EE}} \frac{2c}{-b + \sqrt{b^2 - 4ac}} \qquad \text{if} \quad \overline{y} \leq \overline{y}_{\text{u}}$$
 (5)

$$\widetilde{p}_{\text{EE}} = \widetilde{p}_{\text{u,EE}}$$
 if  $\overline{y} \ge \overline{y}_{\text{u}}$  (6)

Where  $a = 1 - 2n_R$ 

$$b = 2n_{
m R} rac{\overline{oldsymbol{y}}}{\overline{oldsymbol{y}}_{
m u}} - (1-n_{
m R}) \left(1 + rac{\overline{oldsymbol{y}} k_{
m R}}{\widetilde{oldsymbol{p}}_{
m u,EE}}
ight)$$

$$c = rac{\overline{y}k_{
m R}}{\widetilde{p}_{
m u, FE}}(1-n_{
m R}) - n_{
m p}rac{\overline{y}^2}{\overline{
m v}_{
m u}^2}$$

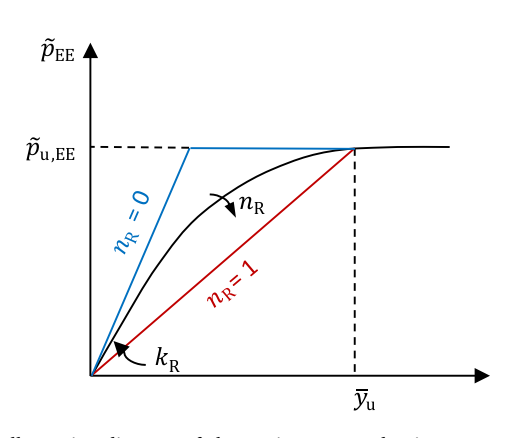


Fig. 11. Illustrative diagram of the conic curve and primary governing parameters used to define the end effect of ROBOCONE p-y module.

Fig. 11 illustrates the shape of the conic function and its four primary variables ( $k_{\rm R}$ ,  $\widetilde{p}_{\rm u,EE}$ ,  $n_{\rm R}$ ,  $\overline{y}_{\rm u}$ ) that depend on sand relative density and surcharge pressure as discussed later. Each of these variables in the conic function has straight-forward interpretation. For instance, the variable  $k_{\rm R}$  controls the initial slope, while  $\overline{y}_{\rm u}$  is the normalised displacement at which the normalised ultimate soil reaction  $\widetilde{p}_{\rm u,EE}$  is attained. Beyond  $\overline{y}_{\rm u}$ , the  $\widetilde{p}_{\rm u,EE}$  remains constant. The  $n_{\rm R}$  (0  $\leq n_{\rm R} \leq$  1) influences the shape of the curve; for  $n_{\rm R}=0$  or 1.0, the function reduces to the bilinear forms, as seen in Fig. 11.

The end effect model operates by correlating the four variables in Equations (5) and (6) with the surcharge pressure and relative density, both of which can be estimated from the processing of regular CPT results. The calibration of the model followed a two-stage optimisation process, as outlined in the flow chart given in Fig. 12, similar to previous work regarding the development of p-y models for monopiles (Burd et al. 2020)

Stage 1 — Step 1: In the first-stage optimisation, the set of variables

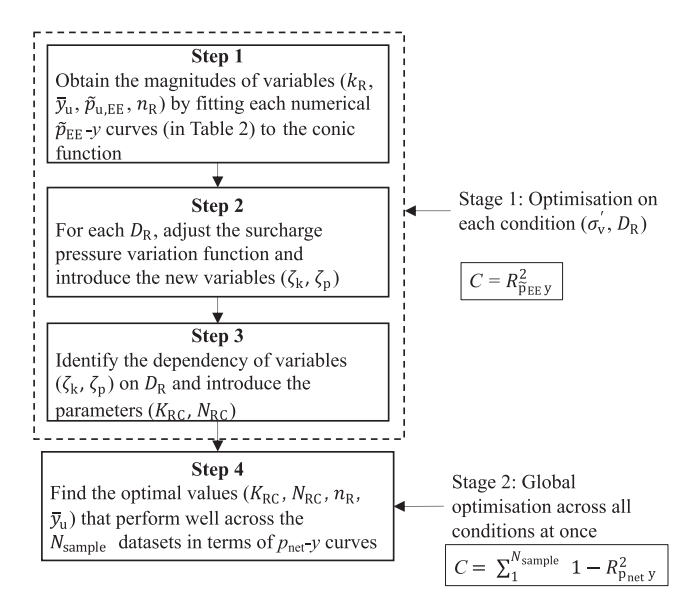


Fig. 12. Two-stage optimisation process for calibration of end effect model.

 $(k_{\rm R},\widetilde{p}_{\rm u,EE},n_{\rm R},\overline{y}_{\rm u})$  was calculated independently for each individual  $\widetilde{p}_{\rm EE}-y$  curve (from Table 2) by minimising the least-square error  $(R_{\widetilde{p}_{\rm EE}}^2)^2$  between the numerical data and the conic function. This process was achieved using optimisation function namely fmincon() in MATLAB (MathWorks Inc. 2022). Prior to optimisation, the initial value of  $k_{\rm R}$  was approximated as the secant stiffness at  $\overline{y}=1$  %, while the  $\widetilde{p}_{\rm u,EE}$  was initially assumed to be the final increment of the numerical  $\widetilde{p}_{\rm EE}$ -y curves. In addition, the curvature variables  $n_{\rm R}$  was subjected to an upper limit of 1.0. An arbitrary  $\overline{y}_{\rm u}$  values of 1.0 was adopted initially and adjusted during optimisation.

**Stage 1** — **Step 2:** For each calibration relative density case, the dependency of the variables  $(k_{\rm R}, \widetilde{p}_{\rm u,EE}, n_{\rm R}, \overline{y}_{\rm u})$  determined from Step 1 on the surcharge pressure  $(\sigma'_{\rm v})$  was separately identified and predicted by the 'surcharge pressure variation function', with new variables  $(\zeta_{\rm k}, \zeta_{\rm p})$  being introduced.

**Stage 1** — **Step 3:** The dependency of new introduced variables ( $\zeta_k$ ,  $\zeta_p$ ) on relative density ( $D_R$ ) was identified and predicted by the 'relative density variation function', with new parameters ( $K_{RC}$ ,  $N_{RC}$ ) being defined.

**Stage 2** — **Step 4:** the aim of the second-stage optimisation is to find the optimised values of ( $K_{RC}$ ,  $N_{RC}$ ,  $n_R$ ,  $\bar{y}_u$ ) that perform well across the entire database to predict the  $p_{net}$ -y curves. The parameters in the surcharge pressure and relative density variation functions were optimised, and the parameter magnitudes from the first-stage calibration were used as initial values.

#### 3.4. Calibration of the model: Stage 1

Fig. 13 shows an example of the individual fitting of the  $\widetilde{p}_{EE}$ -y curves for  $D_R=83\%$ , achieving close agreement with an  $R^2$  of 0.99. While not shown here, the other simulations for the cases in Table 2 also demonstrate excellent matches to numerical data.

The set of primary model parameters determined for all twelve calibration cases are shown as a function of the surcharge pressures  $(\sigma_v^{'})$ , which varies with the depths of p-y module test. Most calibrated  $\overline{y}_u$  parameters are close to 3 (Fig. 14a), irrespective of surcharge stress and density, except two cases under  $\sigma_v^{'}=10$  kPa, 50 kPa where  $\overline{y}_u$  values are smaller. This value represents the displacement at which the  $p_{EE}$  value becomes constant, but could not be verified explicitly, as the simulations only extend to  $y/D_R=0.35$ , and the prototype p-y module has a translation limit of 20 %~25 % $D_R$  (Creasey et al., 2023).

The initial stiffness  $k_R$  increases with both surcharge pressure and

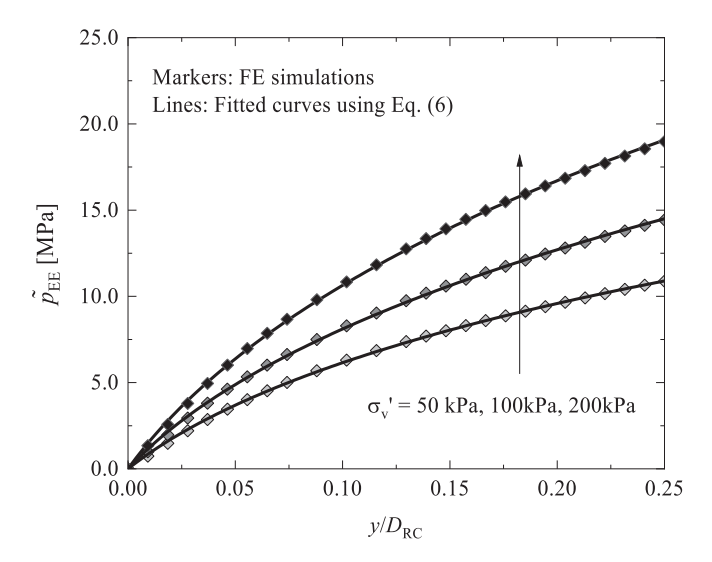


Fig. 13. Individual fitting performance of the conic function to numerial results ( $D_{\rm R}=83\%$ ).

sand density (Fig. 14(b)), as would be expected from the SANISAND-MS model where the shear modulus changes with the confining stress (p') to the power of 0.5 (see Equation (1)). To be consistent, it was assumed that the stiffness parameter  $k_{\rm R}$  would increase according to the same trend,

$$k_{\rm R} = \zeta_{\rm k} p_{\rm atm} \left( \frac{\dot{\sigma_{\rm v}}}{p_{\rm atm}} \right)^{0.5} \tag{7}$$

where  $p_{\text{atm}}$  is atmosphere pressure.  $\zeta_k$  is a variable dependent on relative density  $(D_R)$ , to be optimised according to Step 3.

The curvature parameters  $n_R$  for both loose sand ( $D_R=43\%$ ) and medium dense sand ( $D_R=65\%$ ) fall within the range of 0.8–0.9, indicating slight variation with  $\sigma_v'$  (see Fig. 14c). Conversely, the  $n_R$  values of dense sand show an apparent growth with the surcharge pressure. However, the  $n_R$  values seem to converge as the surcharge pressure increases irrespective of the density. For simplicity, in view of the limited value range and convergence observed, it was considered that this value could be kept constant in Step 3.

The derived ultimate end resistances at corresponding  $\bar{y}_u$  also increase with the surcharge pressure and relative density (Fig. 14(d)). A fitting equation similar to the stiffness parameter was adopted:

$$\widetilde{p}_{\text{u,EE}} = \zeta_{\text{p}} p_{\text{atm}} \left( \frac{\dot{\sigma_{\text{v}}}}{p_{\text{atm}}} \right)^{0.5} \tag{8}$$

Where  $\zeta_p$  is a parameter associated with relative density, which will be optimised in Step 3.

Equations (7) and (8) introduce the new variables ( $\zeta_k$ ,  $\zeta_p$ ), which are correlated to the relative density of the sand as shown in Fig. 15 and Fig. 16. A simple relative density variation function was established as:

$$\zeta_{\rm k} = K_{\rm RC} D_{\rm R}^2 \tag{9}$$

$$\zeta_{\rm p} = N_{\rm RC} D_{\rm R}^2 \tag{10}$$

where  $K_{RC}$  is the non-dimensionless stiffness factor (= 1.82E3 in this case) and  $N_{RC}$  is the so-called bearing factor (= 470), both of which are determined from least-square fitting. The values of  $D_R$  are expressed as a decimal rather than a percentage.

# 3.5. Calibration of the model: Stage 2

Equations (5)-(10) constitute the initial end effect model after the first-stage optimisation. They assume that two variables can be considered constant ( $\bar{y}_u$  and  $n_R$ ) and introduce two parameters ( $K_{RC}$  and  $N_{RC}$ ) in the simplified equations. In the second-stage optimisation, these parameters were updated by minimising the following cost function (C),

$$C = \sum_{1}^{N_{\text{sample}}} 1 - R_{(p_{\text{net}}y)}^{2} \tag{11}$$

where  $N_{\rm sample}=12$  represents the number of datasets in the calibration space. For this second stage optimisation, it was chosen to minimise the error between the numerical  $p_{\rm net}$ -y curves and the predicted  $p_{\rm net}$ -y curves obtained once the ROBOCONE curves are corrected by the end effect model. This choice was made because the  $p_{\rm net}$ -y curves represent the desired outcome of the ROBOCONE interpretation, so these provide the best measure of accuracy.

The initial values of the optimised parameters  $(\bar{y}_u, n_R, K_{RC}, N_{RC})$  were obtained from the first-stage optimisation and all parameters were allowed to vary by up to  $\pm$  50 % of their initial values, subject to an upper limit of 1.0 on the curvature parameter  $n_R$ . This global optimisation led to an updated final set of parameters ( $K_{RC}=2.36E3, \bar{y}_u=3.0, n_R=0.74, N_{RC}=433$ ).

# 3.6. Performance assessment of the end effect model

First, the prediction performance of the developed end effect model

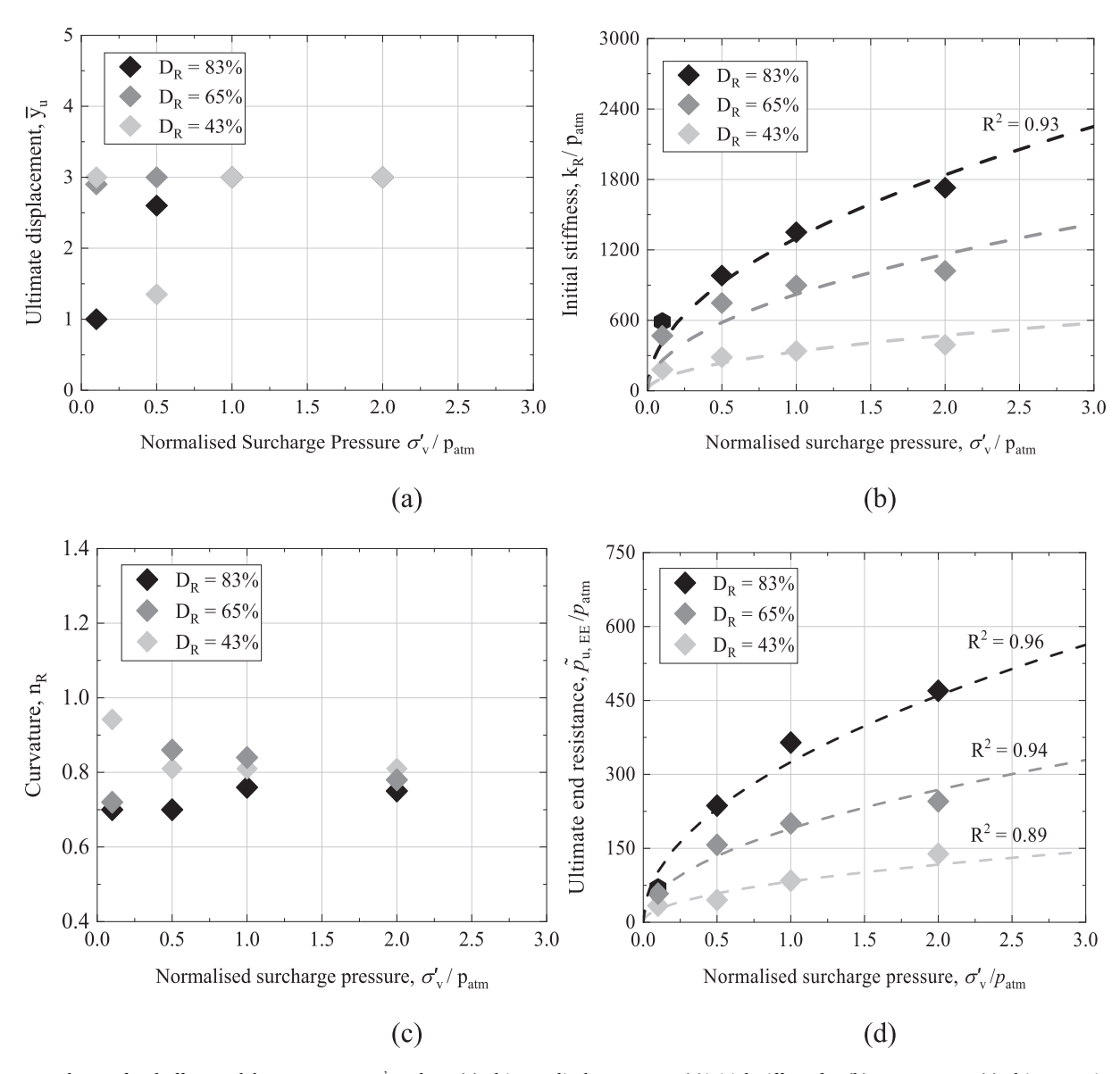


**Fig. 14.** Dependency of end effect model parameters on  $\sigma_{v}$  and  $D_{R}$ : (a) ultimate displacement  $y_{u}$ ; (a)initial stiffness  $k_{R}$ ; (b) curvature  $n_{R}$ ; (c) ultimate resistance  $p_{u,EE}$ 

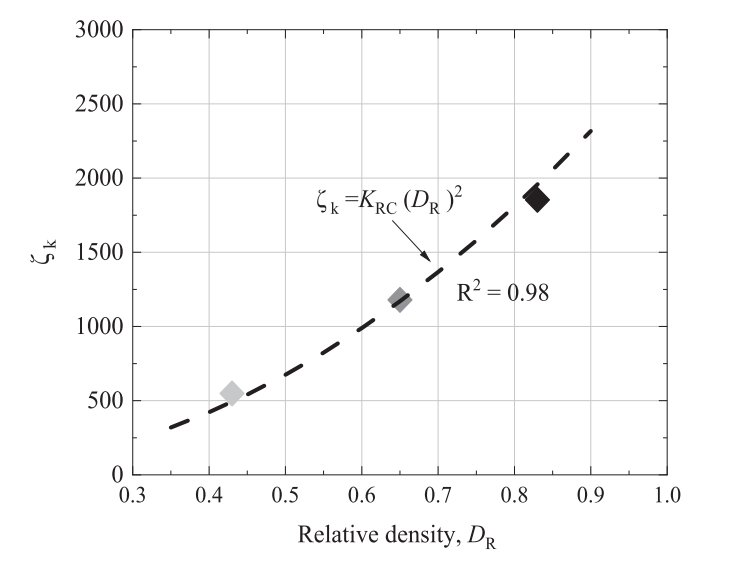


Fig. 15. Power law relationship between  $\zeta_k$  and relative density  $D_R$ 

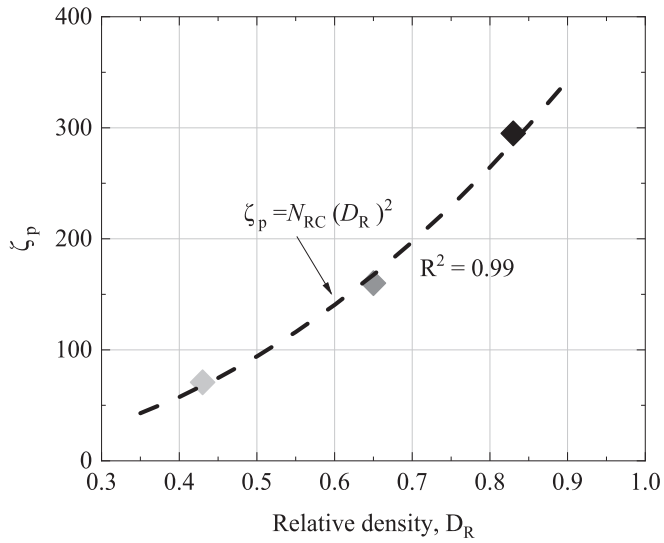


Fig. 16. Relationship between  $\zeta_{\rm p}$  and relative density  $D_{\rm R}$ 

is assessed over the range of calibration conditions (see Table 2). The  $\widetilde{p}_{\text{EE-}}\gamma$  curves were predicted using Equations (5)-(10), whereas the  $p_{\text{net-}}\gamma$  curves were calculated by subtracting the end effects from the direct measurement of p-y module. These two curves were compared to the numerical  $p_{\text{net-}}\gamma$  response and the  $\widetilde{p}_{\text{EE-}}\gamma$  response. Table 3 summarises the performance metric  $R^2$  for all calibration conditions. The average  $R^2$  values of 0.8 and 0.9 respectively indicate a good fit of the developed end effect model to the data, with the higher relative density cases tending to produce slightly higher  $R^2$  than the lower relative density cases.

To further validate the predictive capability of the end effect model, two additional FE cases were performed at a relative density of 55%, with surcharge pressures of  $\sigma_{\rm v}'=75$  kPa and 150 kPa, respectively. These conditions fall within the original calibration space but differ from the conditions employed for the calibration. Fig. 17 shows the  $p_{\rm net}$ -y curves and  $\widetilde{p}_{\rm EE}$ -y curves from numerical FE analysis, together with predictions using the developed end effect model. Values of  ${\rm R}^2$  for two cases indicate a close match between the numerical data and the predictions in terms of both the  $\widetilde{p}_{\rm EE}$ -y curves and the  $p_{\rm net}$ -y curves. This confirms the applicability and robustness of the model developed in this study.

# 4. Applicability of the developed end effect model

The main contribution of this work is to establish a generalised framework to quantify and correct the ROBOCONE data for end effects and determine p-y curves directly for offshore foundation design. This framework is applicable to a wider range of sand types and states, even if the model has been calibrated here using Dunkirk sand constitutive model parameters and a specific prototype ROBOCONE module ( $H_{\rm RC}/D_{\rm RC}=3.7$ ). In the future, the end effect model parameters can be refined as data from the field and additional simulations become available, to build confidence and reduce uncertainty in the correction factors for the ROBOCONE module, so that no further numerical simulations are necessary to interpret the data. In this way, the end effect model as presented here has similar status to equivalent correction factors and empirical correlations for other field-testing methods that often used without soil type-specific calibration (Yu 2006; Suryasentana and Lehane 2014).

However, if required, it would be possible to derive end effect model parameters tailored to a significantly different soil type – such as highly compressible carbonate sands – by rerunning a similar set of FE analyses encompassing the expected density range and stress levels. Once the end effect model is established, it enables corrections to ROBOCONE's insitu measurement of total resistances against displacement, facilitating the generation of net resistance-displacement curves without any end effects. Considering the failure mechanism around ROBOCONE is similarly to the one that can be observed around laterally loaded piles (Wen et al., 2025), these net resistance-displacement curves can be further

**Table 3**Summary of performance metrics of end effect model.

Relative density $D_R$ $(e_0)$	Surcharge pressure $\sigma_{ m v}^{}$ [kPa]	$R^2$ $\widetilde{p}_{\text{EE}}$ -y curves)	R <sup>2</sup> (p <sub>net</sub> -y curves)
83% (0.60)	10	0.98	0.958
	50	0.97	0.972
	100	0.994	0.996
	20	0.965	0.982
65%(0.67)	10	0.764	0.591
	50	0.971	0.983
	100	0.839	0.924
	200	0.591	0.844
43%(0.75)	10	0.963	0.966
	50	0.853	0.936
	100	0.731	0.906
	200	0.692	0.896
Average R <sup>2</sup>	_	0.86	0.91

scaled up to determine the p-y curves for offshore pile design. However, this is beyond the scope of this study.

## 5. Summary & concluding remarks

This study presents an interpretative framework for a new CPT module designed to probe the soil in a manner analogous to the soil surrounding laterally loaded piles. The framework eliminates the end effect of this device caused by its finite length, and reliably convert the in-situ measured response into p-y curves. The 3D finite element approach is used to simulate the behaviour of p-y module in drained sands, with the soil characterised by a bounding surface plasticity model capable of capturing the dependence of sand behaviour on relative density and stress levels. In order to visualise the end effect of the p-y module, two types of FE analyses were undertaken. In Case A, the lateral displacement is solely prescribed on the p-y module, whereas in Case B the same displacement is applied at both p-y module and CPT shaft. Therefore, the ROBOCONE additive resistances due to end effect are determined by deducting the net ROBOCONE resistances (Case B) from the total ROBOCONE resistances (Case A). The following conclusions are reached:

- (a) The end effect becomes less important with increasing aspect ratio of the p-y module as the shaft resistance increasingly dominates the overall response.
- (b) The ratio of end resistance to total resistance is larger under lower surcharge pressure, so a higher correction is required; this ratio also varies with the relative density of the sand.
- (c) The end effect model is developed through a two-stage optimisation on the basis of four-parameter conic function, which captures the effects of relative density and surcharge pressure.
- (d) The developed end effect model can not only reproduce well the behaviour of the ROBOCONE p-y module under calibrated conditions, as indicated by the calculated error measures, but demonstrates general applicability for other validation cases that fall within the calibration space but have different from the initial conditions.
- (e) While the end effect model in this study is based on a specific aspect ratio, the framework proposed in this study to optimise the model parameters can be applied to a p-y module with other aspect ratios.

In summary, this study provides the interpretation framework required to convert the results from the p-y module to the *p-y* curves for pile design. This supports greater use of such in-situ test data for offshore design, without recourse to subsequent onshore laboratory testing, and therefore contributes towards shorter timeframes for offshore project developments. Future work will extend the current monotonic end effect model by incorporating complex cyclic loading conditions. This will leverage the advantages of memory surface components within the SANISAND-MS model.

## CRediT authorship contribution statement

Kai Wen: Writing – original draft, Validation, Methodology, Investigation, Data curation. David J. White: Writing – original draft. Benjamin Cerfontaine: Writing – review & editing, Supervision, Methodology, Funding acquisition, Data curation. Susan Gourvenec: Writing – review & editing, Supervision, Resources, Project administration, Methodology, Funding acquisition. Andrea Diambra: Writing – review & editing, Supervision, Project administration, Methodology, Investigation, Funding acquisition.

# Declaration of competing interest

The authors declare that they have no known competing financial

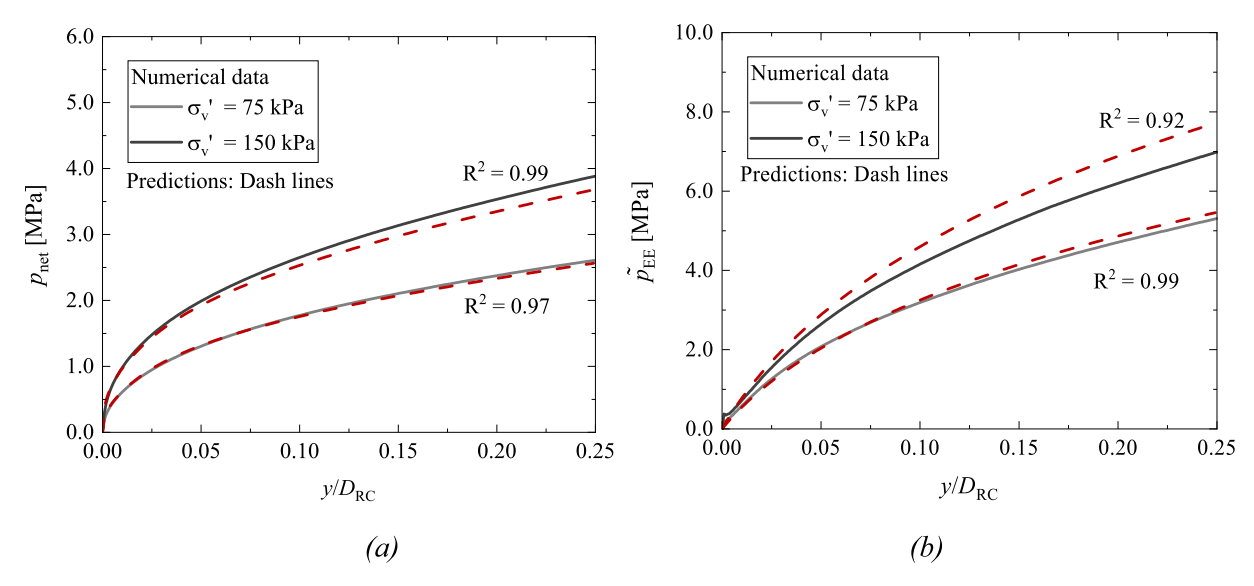


Fig. 17. Performance of end effect model for additional validation cases: (a)  $p_{\text{net}}$ -y curves; (b)  $p_{\text{EE}}$ -y curves.

interests or personal relationships that could have appeared to influence the work reported in this paper.

## Acknowledgement

The authors would like to acknowledge the financial support from the Engineering and Physical Sciences Research Council (Ref: EP/W006235/1: ROBOCONE – intelligent robotics for next generation ground investigation and design) and Science Foundation Ireland (SFI - Ref: 21/EPSRC/3787). Susan Gourvenec is supported through the Royal Academy of Engineering Chair in Emerging Technologies Scheme. David White is also supported through the EPSRC Offshore Renewable Energy Supergen Hub (EPSRC – Ref: EP/Y016297/1).

# Data availability

Data will be made available on request.

### References

API (2014). Recommended Practice 2GEO-Geotechnical and Foundation Design Considerations, American Petroleum Institute. Washington, DC, USA: American Petroleum Institute.

Burd, H.J., Taborda, D.M., Zdravković, L., Abadie, C.N., Byrne, B.W., Houlsby, G.T., Potts, D.M., 2020. PISA design model for monopiles for offshore wind turbines: application to a marine sand. Géotechnique 70 (11), 1048–1066.

Climate Change Committee (2020). The Sixth Carbon Budget: the UK's path to Net Zero (London, UK).

Creasey, J. et al. (2023). Motivation and demonstration of robotic tolling for ground characterisation: the ROBOCONE. Proceedings of the 9th Int. Conf. on Offshore Site Investigations and Geotechnics, pp. 368-375. London, UK: Soc. Underwater Tech.

Dafalias, Y.F., Manzari, M.T., 2004. Simple plasticity sand model accounting for fabric change effects. Journal of Engineering Mechanism. 130 (6), 622–634.

Diambra, A., Creasey, J., Leonet, J., Conn, A., Ibraim, E., Mylonakis, G., White, D., Cerfontaine, B., Gourvenec, S., & Igoe, D. (2022). Concept design of a new CPT module for direct in situ measurement of py soil responses. In *Cone Penetration Testing* 2022 (pp. 900-906). CRC Press.

DNV GL (2016). DNVGL-ST-0126 – Support structure for wind turbines. Oslo, Norway: DNV GL.

Greaves, D., White, D., Noble, D., Jeffrey, H., Gilbert, J., Zhao, X., Byrne, B., Willden, R., Stallard, T., Mullings, H., Scott, B., Brennan, F., Thies, P., Richards, L., Henderson, K., Mascall, R., 2024. ORE Outlook 2040 - UK Offshore Renewable Energy in 2040. Building a Sustainable and Competitive ORE Sector on a Pathway to Net Zero by 2050. Report by Supergen Offshore Renewable Energy Hub.

Guo, F., Lehane, B.M., 2016. Lateral response of piles in weak calcareous sandstone. Can. Geotech. J. 53 (9), 1424–1434. Jeanjean, P., 2009. Re-assessment of P–Y curves for soft clays from centrifuge testing and finite element modeling. In: Offshore technology conference.

Kuwano, R., 1999. The stiffness and yielding anisotropy of sand. PhD thesis. Imperial College, University of London, London, UK.

Lehane, B.M. (2019). CPT-based design of foundations. E.H. Davis Memorial Lecture (2017), Australian Geomechanics, 54(4), 23-48.

Li, X.S., Dafalias, Y.F., 2002. Constitutive modelling of inherently anisotropic sand behaviour. Journal of Geotechnical and Geoenvironmental engineering 128 (10), 868–880.

Liu, H.Y., Abell, J.A., Diambra, A., Pisanò, F., 2019. Modelling the cyclic ratcheting of sands through memory-enhanced bounding surface plasticity. Géotechnique 69 (9), 783–800

Mahmoodzadeh, H., Wang, D., Randolph, M.F., 2015. Interpretation of piezoball dissipation testing in clay. Géotechnique 65 (10), 831–842.

MathWorks Inc. (2022). Statistics and Machine Learning Toolbox Documentation, Natick, Massachusetts: The MathWorks Inc.

Matlock, H. (1970). Correlations for design of laterally loaded piles in soft clay.

Proceedings of the 2nd annual offshore technology conference, Houston, TX, USA, vol. 1, paper no. OTC 1204, pp. 577–594.

Pisanò, F., Del Brocco, I., Ho, H.M., Brasile, S., 2024. 3D FE simulation of PISA monopile field tests at Dunkirk using SANISAND-MS. Géotechnique Letters 1–30.

PLAXIS, 2023. PLAXIS 3D Reference Manual. PLAXIS, Delft, the Netherlands.

Randolph, M.F., Andersen, K.H., 2006. Numerical simulation of T-bar penetration in soft clay. Numerical analysis of T-bar penetration in soft clay. Int. J. Geomech. 6 (6), 411–420

Reese, L.C., Cox, W.R., Koop, F.D. (1974). Analysis of laterally loaded piles in sand. In: Proc., 6th Offshore Technology Conf., Houston, OTC-2080-MS, 473-483.

Stanier, S.A., White, D.J., 2015. Shallow penetrometer penetration resistance. Journal of Geotechnical and Geoenvironmental Engineering 141 (3), 04014117.

Suryasentana, S., Lehane, B.M., 2014. Numerical derivation of CPT-based p-y curves for piles in sand. Géotechnique 64 (3), 186–194.

Wang, Y., Hu, Y., Hossain, M.S., Zhou, M., 2020. Effect of trapped cavity mechanism on interpretation of T-Bar penetrometer data in uniform clay. J. Geotech. Geoenviron. Eng. 146 (9), 04020078.

Wen, K., Cerfontaine, B., White, D., Gourvenec, S., Diambra, A., 2024. Lateral bearing factors and elastic stiffness factors for robotic CPT py module in undrained clay. *Comput. Geotech.* 172, 106487.

Wen, K., White, D., Cerfontaine, B., Gourvenec, S., Diambra, A., 2025. In: A new robotic CPT p-y module for offshore seabed characterisation and offshore pile design. 5th International Symposium on Frontiers in Offshore Geotechnics, Nantes, France.

White, D. J. (2022). CPT equipment: Recent advances and future perspectives. In Cone Penetration Testing 2022, (pp. 66-80). CRC press.

Yan, Y., White, D.J., Randolph, M.F., 2011. Penetration resistance and stiffness factors for hemispherical and toroidal penetrometers in uniform clay. *Int. J. Geomechanics* 11 (4), 263–275.

Yu, H.S., 2006. The First James K. Mitchell Lecture In situ soil testing: from mechanics to interpretation. *Geomech. Geoeng.* 1 (3), 165–195.

Zdravković, L., Jardine, R. J., Taborda, D. M. G., Burd, H. J., Byrne, B. W., Gavin, K. G., Houlsby, G. T., Igoe, D. J. P., Liu, T., Martin, C. M., McAdam, R. A., Muir Wood, A., Potts, D. M., Skov Gretlund, J. & Ushev, E. (2020). Ground characterisation for PISA pile testing and analysis. *Géotechnique*. 70(11), 945-960.

Zhou, M., Hossain, M.S., Hu, Y., Liu, H., 2013. Behaviour of ball penetrometer in uniform single-and double-layer clays. Géotechnique 63 (8), 682–694.